

Determining stellar accretion rates from Pa_α and Br_β emission lines with JWST NIRSpec.

Accretion of pre-main-sequence stars in NGC 3603

Ciarán Rogers¹, Guido de Marchi², Bernhard Brandl^{1,3}

¹ Leiden Observatory, Leiden University, PO Box 9513, 2300 RA Leiden, The Netherlands
e-mail: rogers@strw.leidenuniv.nl

² European Space Research and Technology Centre, Keplerlaan 1, 2200 AG Noordwijk, The Netherlands
e-mail: gdemarchi@rssd.esa.int

³ Faculty of Aerospace Engineering, Delft University of Technology, Kluyverweg 1, 2629 HS Delft, The Netherlands

Received January 19 2024; accepted March 11 2024

ABSTRACT

In this Letter, we present the first systematic spectroscopic measurements of the near-infrared (NIR) hydrogen recombination lines Paschen alpha (Pa_α , $\lambda = 1.875\mu\text{m}$) and Brackett beta (Br_β , $\lambda = 2.626\mu\text{m}$), produced by pre-main-sequence (PMS) stars. Such stars include T Tauri and Herbig AeBe stars, located in the massive Galactic star-forming region NGC 3603. We used measurements obtained from JWST NIRSpec, using multi-object spectroscopy (MOS) mode. Based on the existing empirical relations between L_{acc} and L_{Br_γ} from the literature, we used our new measurements to formulate, for the first time, an empirical relationship between the accretion luminosity, L_{acc} , of the stars and the line luminosities, L_{line} , of both Pa_α and Br_β . These relationships are: $\log_{10}(\frac{L_{acc}}{L_\odot}) = 1.42(\pm 0.18) \times \log_{10}(\frac{L_{Pa_\alpha}}{L_\odot}) + 3.33(\pm 0.42)$ and $\log_{10}(\frac{L_{acc}}{L_\odot}) = 1.47(\pm 0.18) \times \log_{10}(\frac{L_{Br_\beta}}{L_\odot}) + 4.60(\pm 0.57)$. These new relationships are key to establishing rough estimates of the accretion rates for large samples of PMS stars with JWST.

Key words. Stars: formation - (Stars:) circumstellar matter - Stars: pre-main-sequence

1. Introduction

The accretion luminosity, L_{acc} , of a star is a direct measurement of the gravitational energy released by infalling matter as it is accreted. If the mass, M_* , and radius, R_* , are known, then the mass accretion rate, \dot{M}_* , can be determined from L_{acc} . The mass accretion rate is a fundamental characteristic of star formation, setting important constraints on accretion and stellar evolution models Calvet et al. (1999). It is also a crucial aspect of disk evolution and star and planet formation (Muzerolle et al. 1998; Basri & Bertout 1989). The accretion luminosity of a star is primarily radiated at ultraviolet (UV) and blue and optical wavelengths, producing excess emission above the intrinsic photospheric level of the star (e.g. Calvet & Gullbring 1998). It is possible to measure this accretion luminosity directly by observing the excess UV and optical continuum emission and comparing it to an appropriate stellar photosphere. This is commonly done using U and B band photometry with complementary spectroscopy, (e.g. Venuti et al. 2014; Herczeg & Hillenbrand 2008; Gullbring et al. 1998).

Another approach to measuring the accretion luminosity is to use hydrogen recombination lines. The accretion luminosity has been shown to scale linearly with various recombination line luminosities. In Muzerolle et al. (1998), they found that the NIR hydrogen recombination line Br_γ ($\lambda = 2.166\mu\text{m}$) exhibited a tight scaling relationship with the accretion luminosity of 19 pre-main-sequence (PMS) stars. Such close relationships have since been found for a wide range of lines from hydrogen, as well as other elements (e.g. Alcalá et al. 2017).

The motivation behind using NIR recombination lines is two-fold. Firstly, NIR lines suffer from ~ 10 times less extinction compared to UV and optical wavelengths. This results in a higher signal-to-noise ratio (S/N), making it possible to measure the accretion rates of more deeply embedded and/or distant objects. Secondly, because the extinction is lower, uncertainties that arise from extinction corrections are also smaller.

The majority of NIR stellar accretion studies have been conducted from ground-based observatories. From the ground, the strong recombination lines Pa_α and Br_β are not visible due to telluric contamination. Using the JWST Near InfraRed Spectrograph (NIRSpec), we were able to obtain moderate-resolution ($R = 2700$) spectra for 100 stars, 32 of which we classified as PMS stars. The grating-and-filter combination of $G235H/F170LP$ was used. This gives us access to recombination lines that are not observable from the ground: Pa_α , a line that is typically ~ 12 times brighter than Br_γ , and Br_β , typically ~ 1.6 times brighter than Br_γ . These lines provide a new means to measure the accretion luminosity of PMS stars in the era of JWST, offering higher S/N, coupled with the exquisite sensitivity of NIRSpec, thus allowing for deeper and more precise star formation studies. The layout of this paper is as follows. In Section 2, we discuss the sample and our target selection criteria. In Section 3, we discuss the data processing steps, including the data reduction, extinction correction, flux calibration, photospheric and veiling corrections, and the measurement of the recombination lines. In Section 4 we present our results and in

Section 5 we summarise our findings and present our conclusions.

2. Targets

The spectra were obtained as part of a NIRSpec Guaranteed Time Observations (GTO) programme (ID=1225). The stars reside in the giant Galactic HII region NGC 3603, located 7 ± 1 kpc away (Melena et al. 2008; Sung & Bessell 2004; Pandey et al. 2000). The cluster's age has been estimated to be 1–3 Myr (Pang et al. 2013; Sung & Bessell 2004; Melena et al. 2008), with active ongoing star formation Beccari et al. (2010) (B10). The spectra were obtained using the MOS mode of NIRSpec, which utilises the Micro-Shutter Assembly (MSA). The MSA consists of $\sim 250\,000$ microscopic, operable doors that can be commanded open or closed, allowing for the simultaneous acquisition of dozens of spectra within a single exposure Ferruit et al. (2022). These targets were chosen from an initial list of about 10 000 sources, originally observed with Hubble Space Telescope's (HST) Wide Field Camera 3 (WFC3), see (B10). Of the 100 sources observed with JWST, 60 were photometrically classified as PMS stars based on $H\alpha$ narrow band excess emission; the remaining 40 stars were classified as main-sequence (MS) stars.

With our new spectroscopic data, we have revised this classification. We have classified 32 of the 100 sources as PMS. This lower classification rate likely comes from our stricter criteria. Following our classification criteria, a source was deemed PMS based on the simultaneous presence of the recombination lines: Pa_α , Br_β , and Br_γ , in emission above the chromospheric level, after a photospheric absorption correction had been performed (see Section 3.5.2). There are sources in our sample that exhibit only a subset of these lines in emission, in most cases, only Pa_α . We have excluded these sources from our analysis simply because it is not possible to draw a relationship between Br_γ and the other recombination lines if Br_γ is not seen in emission. It is entirely possible that there are additional PMS sources in our sample, but within the scope of this study, we have focused on sources with strong recombination lines, unambiguously in emission. Of the 32 sources that we classified as PMS, 21 had also been classified in (B10) as PMS based on $H\alpha$ excess. The remaining 12 sources did not show evidence of $H\alpha$ excess at the time the observations were made. Differences in the nebular background subtraction, extinction correction and photospheric correction could explain the differences between our classification and (B10). There is also a ~ 13 year time gap between our NIRSpec measurements and the photometric measurements of (B10); thus, variability could also play a role. The sources are listed in Table 1 with their positions, physical properties, recombination line equivalent widths (EWs), and accretion luminosities.

It is possible for recombination lines to be present in MS/evolved sources through chromospheric emission (Herbig 1985; Strassmeier et al. 1990; Young et al. 1989). Chromospheric activity can be confused for weak accretion, as both mechanisms produce emission lines with small EWs. Accretion is usually associated with large EWs, for example: $H_\alpha \geq 10\text{\AA}$. This corresponds to EWs for Pa_α and Br_β of 1.2\AA and 0.15\AA , respectively, assuming case B recombination Hummer & Storey (1987). To avoid any misclassifications, we have taken a conservative approach and only considered sources with hydrogen recombination lines whose EWs are ≥ 3 times what is expected from chromospheric activity.

In some of the PMS spectra, there are additional hydrogen recombination lines, from the Brackett series as well as the Pfund series. A full description of the PMS spectra will be given in (Rogers et al. in prep.).¹

We have spectrally classified the majority of the PMS stars in this study. A subset of sources could not be classified spectroscopically as they lack any absorption lines. These PMS stars have temperatures masses estimated photometrically from (B10), ranging from $2 \leq \frac{M_*}{M_\odot} \leq 5.5$, with an uncertainty of the order of $M_* \times \sqrt{2}$, placing them somewhere within the intermediate mass T Tauri, and Herbig AeBe star range. The large uncertainties on mass and temperature prevent us from firmly classifying these sources. In Table 1, we refer to these sources as either TT/H Ae or H Ae/Be stars.

3. Data reduction

3.1. Spectral extraction with NIPS

The data were reduced using the NIRSpec Instrument Pipeline Software (NIPS) Alves de Oliveira et al. (2018). NIPS is a framework for spectral extraction of NIRSpec data from the count-rate maps, performing all major reduction steps from dark current and bias subtraction to flat fielding, wavelength and flux calibration and spectral extraction, with the final product being the 1D extracted spectrum.

3.2. Nebular background subtraction

NGC 3603 is the optically brightest HII region in the Galaxy. As such, the nebular emission of NGC 3603 is extremely bright, in particular with respect to the recombination lines, which have typical EWs of $\sim 5000\text{\AA}$. The nebular emission is also spatially variable across the area of a few micro-shutters (micro-shutter area = $0.46'' \times 0.2'' \sim 10^{-4} pc^2$). The removal of these nebular recombination lines from the stellar spectra was crucial in order to determine accurate accretion luminosities from the genuine stellar recombination lines.

Spectroscopy of the nebula was carried out simultaneously with the stellar spectroscopy. This was done by opening 'slitlets', consisting of three micro-shutters for each stellar source. The star was placed within the central micro-shutter, with the neighbouring shutters directly above and below it observing the adjacent nebular background. From the multiple nebular spectra per stellar source, we observed that the nebular emission line fluxes typically differed by 7% between adjacent micro-shutters. In 5 out of 32 PMS sources, the corresponding nebular emission line fluxes differed by $\geq 20\%$ between adjacent micro-shutters. In these cases, the measured nebular spectrum was likely not representative of the nebulosity within the central micro-shutter; hence, this could lead to over- or under-subtraction.

In order to account for the spatially variable nebulosity, a brightness scaling procedure was developed to subtract the nebular light from the stellar spectrum. In all of the nebular spectra, a bright helium doublet is present at $\lambda = 1.869\mu m$. For our sample of stars, this line has a purely nebular origin, only appearing weakly in absorption ($EW \leq 1\text{\AA}$) in massive stars Husser et al. (2013). The line flux of the helium doublet was measured in the unsubtracted stellar spectrum and the corresponding nebular spectrum was scaled and subtracted from the stellar spectrum, such that the helium line was fully removed. The typical scaling

¹ Individual spectra can be made available by the authors upon request.

ID	RA	DEC	T_{eff} (K)	Group	M_* (M_\odot)	EW Pa_α (Å)	EW Br_γ (Å)	EW Br_β (Å)	$\log_{10}(L_{acc})$ (L_\odot)
727	168.8096466	-61.263581	3800 ±150	TT	0.5 ±0.06	-23.1 ±2.2	-0.8 ±0.2	-9.7 ±1.9	-1.42 ±0.75
654	168.7541941	-61.2514463	4600 ±150	TT	0.75 ±0.07	-3.6 ±0.4	-0.4 ±0.1	-3.8 ±0.7	-1.42 ±0.72
4595	168.8129136	-61.2625111	3600 ±150	TT	0.47 ±0.05	-22.2 ±2	-2.4 ±0.7	-26 ±4.7	-1.4 ±0.74
996	168.7973597	-61.2640824	5200 ±150	TT	0.97 ±0.08	-8.9 ±0.7	-0.5 ±0.2	-2.9 ±0.5	-1.11 ±0.74
1497	168.7688519	-61.25128	6000 ±100	TT	1.3 ±0.04	-24.2 ±2	-2.9 ±0.5	-17.1 ±2.9	-1.08 ±0.71
1457	168.7310205	-61.2672106	5400 ±100	TT	1.05 ±0.04	-45.5 ±3.8	-10.7 ±1.3	-61 ±10.5	-0.75 ±0.69
1038	168.7957658	-61.2643274	5400 ±150	TT	1.05 ±0.08	-54.2 ±4.6	-3.6 ±0.5	-12.2 ±2	-0.75 ±0.68
1339	168.8197744	-61.2630422	4400 ±150	TT	0.7 ±0.06	-12 ±1	-5.7 ±0.7	-45 ±7.8	-0.73 ±0.69
858	168.7365507	-61.2702015	9600 ±200	H Ae/Be	3.3 ±0.14	-82.6 ±6.9	-7.6 ±0.8	-33.5 ±5.9	-0.67 ±0.48
1813	168.8037358	-61.246069	5600 ±150	TT	1.1 ±0.08	-48 ±4.1	-5.6 ±0.7	-38 ±6.7	-0.65 ±0.69
1442	168.8120917	-61.2671703	4200 ±150	TT	0.65 ±0.06	-11 ±0.9	-1 ±0.2	-2.4 ±0.4	-0.65 ±0.69
1997	168.8052566	-61.2510052	4400 ±200	TT	0.7 ±0.06	-14.8 ±1.3	-1.3 ±0.2	-3.2 ±0.6	-0.61 ±0.69
1717	168.8138352	-61.2507679	5800 ±200	TT	1.2 ±0.08	-24.6 ±2.1	-3.4 ±0.6	-6.7 ±1.2	-0.61 ±0.76
4649	168.7420813	-61.2585345	3600 ±150	TT	0.47 ±0.05	-128.7 ±11.7	-10.6 ±1.8	-59.3 ±10.6	-0.53 ±0.67
1271	168.7330151	-61.2635352	4600 ±200	TT	0.75 ±0.07	-70.6 ±6	-9 ±1.1	-17.5 ±3.1	-0.47 ±0.67
2326	168.7438995	-61.2588048	3800 ±150	TT	0.5 ±0.06	-114.3 ±10.1	-25.7 ±4.4	-86.3 ±16.3	-0.41 ±0.67
1134	168.7353906	-61.2705277	5600 ±150	TT	1.13 ±0.08	-125.1 ±10.5	-10.1 ±1.2	-45.4 ±8.1	-0.37 ±0.67
2673	168.7975961	-61.2649162	4400 ±100	TT	0.7 ±0.03	-34.2 ±3	-3.5 ±0.5	-7.3 ±1.4	-0.36 ±0.67
1854	168.7292443	-61.2600537	4200 ±150	TT	0.75 ±0.07	-225.1 ±19.7	-22.8 ±2.9	-127.9 ±22.3	-0.36 ±0.67
2492	168.7427501	-61.2714228	5000 ±100	TT	0.9 ±0.04	-245 ±21.8	-57.6 ±7	-79.2 ±14.7	-0.27 ±0.66
977	168.8092518	-61.2623119	5000 ±150	TT	0.9 ±0.07	-19.1 ±1.6	-2 ±0.3	-5.8 ±1.1	-0.03 ±0.67
354	168.7704651	-61.2626355	10600 ±2000	H Ae/Be	4.02 ^{+1.7} _{-1.2}	-22.5 ±2.1	-5 ±1.3	-5.6 ±1.3	0.07 ±0.49
853	168.7643462	-61.2488318	5400 ±100	TT	1.05 ±0.04	-18.2 ±1.5	-2.1 ±0.3	-5.9 ±0.9	0.15 ±0.64
2166	168.7944201	-61.2661562	5000 ±150	TT	0.9 ±0.07	-69.1 ±6.2	-6.5 ±0.8	-15.3 ±2.6	0.27 ±0.64
152	168.7817328	-61.2648809	9400 ±1800	H Ae/Be	4.33 ^{+1.8} _{-1.3}	-14.9 ±1.2	-1.5 ±0.2	-2.2 ±0.4	0.42 ±0.44
1350	168.8031179	-61.2483281	5000 ±2000	TT/H Ae	0.9 ±0.7	-53.6 ±4.4	-8.2 ±1	-11.1 ±2	0.66 ±0.63
1354	168.7519521	-61.2645637	6600 ±1400	TT/H Ae	2.18 ^{+0.90} _{-1.3}	-20.8 ±1.7	-3.5 ±0.4	-5 ±0.8	0.9 ±0.62
823	168.7623889	-61.2710101	7200 ±1400	H Ae	3.11 ^{+1.3} _{-0.92}	-33.8 ±2.9	-6 ±0.7	-9 ±1.5	1.79 ±0.43
238	168.8151779	-61.2550836	7000 ±1800	H Ae/Be	5.47 ^{+2.3} _{-1.6}	-76 ±6.3	-13.5 ±2.1	-23.6 ±4.2	2.06 ±0.39
185	168.7627924	-61.2625057	8200 ±1800	H Ae/Be	5.06 ^{+2.1} _{-1.5}	-82.2 ±6.8	-9.4 ±1.1	-14.1 ±2.3	2.13 ±0.37
469	168.7941589	-61.2779717	8600 ±1800	H Ae/Be	5.16 ^{+2.1} _{-1.5}	-216.9 ±45.1	-16.2 ±2	-17.2 ±3.1	2.52 ±0.36
251	168.7684956	-61.2531283	6400 ±1800	TT/H Ae	3.74 ^{+1.3} _{-1.1}	-124.9 ±10.6	-13.7 ±1.6	-17.6 ±3.1	2.75 ±0.37

Table 1: Physical properties of the PMS stars considered in this analysis and the EWs of the three recombination lines. The sources have been ordered in terms of increasing accretion luminosity. The Group column indicates whether the sources are classified as T Tauri or Herbig AeBe. For the T Tauri stars, the temperatures, masses and associated uncertainties come directly from the Phoenix stellar models based on the five best fitting model spectra. For the Herbig AeBe stars, the temperatures and masses come from the photometry of (B10). The uncertainty in mass for each source has been calculated based on $M_* \times \sqrt{2}$. The uncertainty in temperature for the Herbig AeBe stars has been determined from the Phoenix models, such that the range of temperatures reproduces the upper and lower mass limit for each source.

Note: Source 1350 could not be classified by spectroscopic or photometric means and so, a temperature of 5000 K was assumed with an uncertainty of 2000 K.

factor was 0.94 ± 0.2 . The typical He I EW after subtraction was $0.011 \pm 0.16\text{Å}$.

We have estimated the uncertainty of this nebular subtraction by comparing the EW of the helium doublet to that of the hydrogen recombination lines of interest, namely Pa_α , Br_γ , and Br_β . The helium and hydrogen lines exhibit a tight scaling relationship with an origin at $\sim 0\text{Å}$. This indicates that by removing the helium line, the hydrogen lines have also been fully subtracted. The dispersion of these relationships for Pa_α , Br_γ , and Br_β were 8%, 11%, and 17%, respectively. These dispersions were taken as the uncertainty of our subtraction for each line and were propagated through to the final line luminosities.

3.3. Extinction correction

The stellar spectra also needed to be corrected for interstellar extinction. The extinction characteristics of NGC 3603 have been explored in detail in (Rogers et al., submitted). This study utilised the hydrogen recombination lines of the nebular spectra. By studying the decrement of the Brackett recombination lines, it was possible to determine the NIR extinction law for each of our sources in NGC 3603, which allowed us to determine the reddening $E(B - V)$ and the absolute extinction $A(V)$ for each

source. Using these values, the stellar spectra were corrected for extinction, and the uncertainties from $R(V)$ and $E(B - V)$ and $A(V)$ were propagated through to the uncertainty of the recombination line luminosities. The typical value of $R(V)$ for the region is $R(V) = 4.8 \pm 1.06$, corresponding to $E(B - V) = 0.64 \pm 0.27$ and $A(V) = 3.1 \pm 1.46$

3.4. Flux calibration

The NIRSpec calibration does not yet offer absolute flux calibrated spectra and so, this must be done with a photometric catalogue. We have used the non-contemporaneous K_s band photometry of Brandl et al. (1999), obtained with ISAAC at the VLT. To avoid the impact of temporal variability from the PMS sources, we used only the MS sources to determine the flux correction. By convolving our JWST MS stellar spectra with the ISAAC K_s throughput filter, we found that our spectra were typically fainter than the corresponding ISAAC fluxes by a factor of 3.69 ± 0.93 . We then applied this correction factor to the 32 PMS spectra. The uncertainty of this flux calibration was propagated through to the uncertainty of the line luminosities.

3.5. Determining L_{Pa_α} and L_{Br_β}

3.5.1. Measuring the recombination line EWs

A Monte Carlo approach was taken to measure the recombination lines, similarly to (Riedel et al. 2017; Ashraf et al. 2023). With this approach, each line was measured 1000 times by fitting a Gaussian to determine the EW of the line. The EW was multiplied by the continuum to convert to a line flux. The line flux was allowed to vary with each iteration within its statistical and systematic uncertainties, under the assumption of independent and normally distributed uncertainties. The median of the 1000 fluxes was calculated and the uncertainty of the line flux was the standard deviation of the 1000 measurements. Figure 1 shows the line profiles of Pa_α , Br_γ , and Br_β from the spectrum of source 977, an intermediate S/N source in our sample. A full grid of line profiles is provided in Section A.

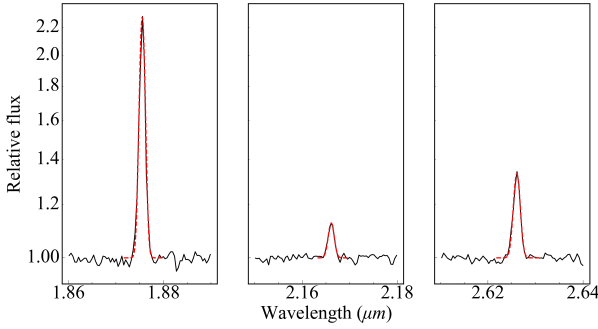


Fig. 1: Three recombination lines: Pa_α , Br_γ , and Br_β are shown going from left to right. These lines come from the spectrum of source 977.

3.5.2. Correcting for photospheric absorption and veiling

Before converting the EW to a flux, each EW needed to be corrected for photospheric absorption and veiling. To correct for photospheric absorption, the spectral type had to be determined. To do so, the Phoenix stellar models from Husser et al. (2013) were fit to the spectra using a minimum χ^2 approach. A combination of hydrogen absorption lines, as well as metal absorption lines from NaI , CaI , AlI , and MgI were used to fit the spectra. An example fit is shown in Figure 2. The uncertainties in T_{eff} , $Log(g)$, and metallicity $[M/H]$ were determined from the standard deviation of the five best fitting models. Once the spectral type was known, the EWs of Pa_α , Br_β , and Br_γ were measured in the model spectra. The EW uncertainties were also determined from the standard deviation of the five best fitting model spectra. For spectra where no absorption lines were detected, we used the spectral types determined by (B10), with their associated uncertainties.

The approach from Lopez et al. (2006) was used to simultaneously correct the spectra for absorption and veiling,

$$EW_{circ} = EW_{obs} - EW_{photo} \times 10^{-0.4 \times \Delta m_K} \quad (1)$$

where EW_{circ} is the true EW of the line emission from the circumstellar disk; EW_{obs} is the measured EW of the line; EW_{photo} is the EW of the photospheric absorption component; Δm_K is the absolute value of the difference between the scaled Phoenix model, K_s , band magnitude and the observed K_s band magnitude. To determine Δm_K , the extinction-corrected K_s band mag-

nitude of the observed spectrum was subtracted from the K_s band magnitude of an appropriate Phoenix stellar model, scaled to the distance of NGC 3603. The absolute value of this difference was used for Δm_K . The corrected EWs were converted to fluxes as described above and, finally, to luminosities by scaling to the distance of 7 ± 1 kpc, and propagating the uncertainty of the distance.

4. Results

4.1. Determining the accretion luminosity relationship for Pa_α and Br_β

To determine the new empirical relationships between L_{acc} and Pa_α and Br_β , we utilised two separate, existing relationships for Br_γ , determined by Alcalá et al. (2017) for T Tauri stars and Fairlamb et al. (2015) for the Herbig AeBe stars, although both relationships actually agree with each other within their uncertainties. These relationships are given in Equation 2 and 3, respectively:

$$\log \frac{L_{acc}}{L_\odot} = 1.19(\pm 0.1) \log \frac{L_{Br_\gamma}}{L_\odot} + 4.02(\pm 0.51), \quad (2)$$

$$\log \frac{L_{acc}}{L_\odot} = 1.30(\pm 0.09) \log \frac{L_{Br_\gamma}}{L_\odot} + 4.46(\pm 0.23). \quad (3)$$

Using the relationships in Equations 2 and 3, we calculated the accretion luminosities of our PMS stars based on their Br_γ line luminosities.

In order to derive the relationships for Pa_α and Br_β , we fit lines between the accretion luminosities and the two recombination line luminosities. The best fitting lines are shown in Figure 3. These fits provide the new empirically derived relationship between the accretion luminosity and Pa_α and Br_β . These relationships are given in Equations 4 and 5:

$$\log_{10} \left(\frac{L_{acc}}{L_\odot} \right) = 1.42(\pm 0.18) \log_{10} \left(\frac{L_{Pa_\alpha}}{L_\odot} \right) + 3.33(\pm 0.42), \quad (4)$$

$$\log_{10} \left(\frac{L_{acc}}{L_\odot} \right) = 1.47(\pm 0.18) \log_{10} \left(\frac{L_{Br_\beta}}{L_\odot} \right) + 4.60(\pm 0.57). \quad (5)$$

The uncertainties of both the slope and y-intercept are dominated by systematic uncertainties. These systematics arise from the absolute flux calibration, the distance to NGC 3603, and the uncertainties inherited from Equations 2 and 3. Taking Equation 4 for instance, the uncertainties can be broken down into their statistical and systematic components, with statistical uncertainty in square brackets and systematic uncertainty in angle brackets: $(\pm 0.18) \rightarrow [\pm 0.006] + \langle \pm 0.174 \rangle$ and $(\pm 0.42) \rightarrow [\pm 0.012] + \langle \pm 0.408 \rangle$.

5. Conclusions

We present the first empirical relationship between L_{acc} and L_{Pa_α} and L_{Br_β} by making use of the existing relationships between L_{acc} and L_{Br_γ} from Alcalá et al. (2017) and Fairlamb et al. (2015). These new empirical relationships should serve star formation studies in the era of JWST, where simultaneous access to these strong NIR lines has been made available for the first time. This will allow for deeper and wider star formation studies at larger distances than has been previously possible.

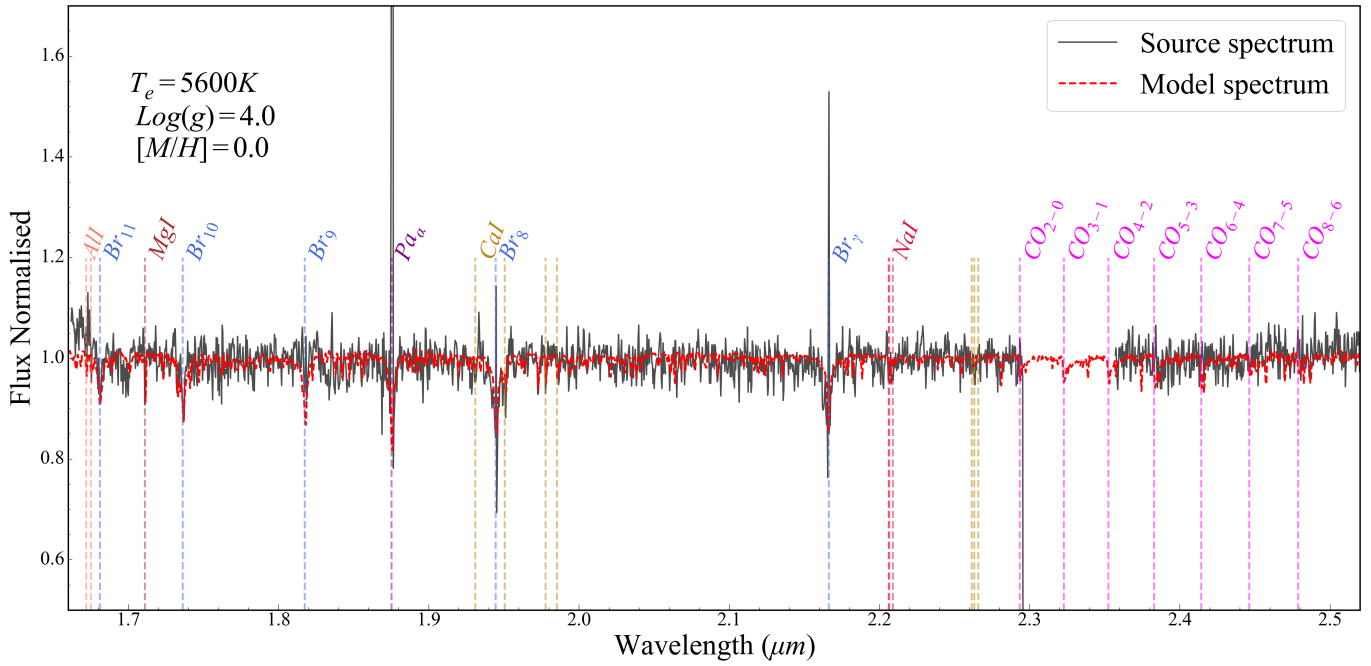


Fig. 2: Best fitting Phoenix model spectrum. The source spectrum is shown as the black solid line. The best-fit model spectrum is shown as the red dashed line.

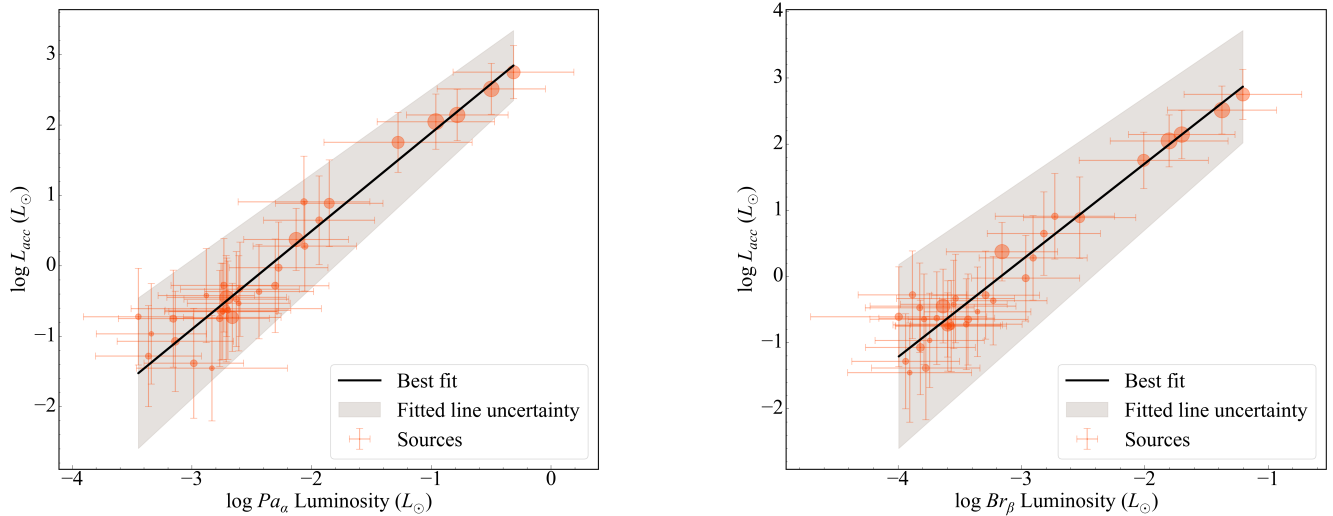


Fig. 3: Relationship between L_{acc} with Pa_α and Br_β . The size of the circle scales with the mass of the source. The black line is the line of best fit, determined via ODR. The grey shaded band is the uncertainty of the best fit line. Panel a: The scatter between data and the line of best fit is $\sigma = 0.27$. Panel b: The scatter between data and the line of best fit is $\sigma = 0.27$.

6. Acknowledgements

We would like thank the referee for their careful consideration of this letter, and for their helpful comments which has improved its quality. We are also grateful to Juan Alcalá and Katia Biazzo for their invaluable help regarding the veiling and photospheric corrections for our data.

References

- Alcalá, J., Manara, C., Natta, A., et al. 2017, *Astronomy & Astrophysics*, 600, A20
- Alves de Oliveira, C., Luetzgendorf, N., Ferruit, P., & Rawle, T. 2018
- Ashraf, M., Jose, J., Herczeg, G., & Fang, M. 2023, *Journal of Astrophysics and Astronomy*, 44, 67
- Basri, G. & Bertout, C. 1989, *Astrophysical Journal*, Part 1 (ISSN 0004-637X), vol. 341, June 1, 1989, p. 340-358., 341, 340
- Beccari, G., Spezzi, L., De Marchi, G., et al. 2010, *The Astrophysical Journal*, 720, 1108
- Brandl, B., Brandner, W., Eisenhauer, F., et al. 1999, arXiv preprint astro-ph/9910238

- Calvet, N. & Gullbring, E. 1998, *The Astrophysical Journal*, 509, 802
- Calvet, N., Hartmann, L., & Strom, S. E. 1999, arXiv preprint astro-ph/9902335
- Fairlamb, J. R., Oudmaijer, R. D., Mendigutia, I., Ilee, J. D., & van den Ancker, M. E. 2015, *Monthly Notices of the Royal Astronomical Society*, 453, 976
- Ferruit, P., Jakobsen, P., Giardino, G., et al. 2022, *Astronomy & Astrophysics*, 661, A81
- Gullbring, E., Hartmann, L., Briceno, C., & Calvet, N. 1998, *The Astrophysical Journal*, 492, 323
- Herbig, G. 1985, *Astrophysical Journal, Part 1 (ISSN 0004-637X)*, vol. 289, Feb. 1, 1985, p. 269-278., 289, 269
- Herczeg, G. J. & Hillenbrand, L. A. 2008, *The Astrophysical Journal*, 681, 594
- Hummer, D. G. & Storey, P. J. 1987, *MNRAS*, 224, 801
- Husser, T.-O., Wende-von Berg, S., Dreizler, S., et al. 2013, *Astronomy & Astrophysics*, 553, A6
- Lopez, R. G., Natta, A., Testi, L., & Habart, E. 2006, *Astronomy & Astrophysics*, 459, 837
- Melena, N. W., Massey, P., Morrell, N. I., & Zangari, A. M. 2008, *The Astronomical Journal*, 135, 878
- Muzerolle, J., Hartmann, L., & Calvet, N. 1998, *The Astronomical Journal*, 116, 2965
- Pandey, A. K., Ogura, K., & Sekiguchi, K. 2000, *Publications of the Astronomical Society of Japan*, 52, 847
- Pang, X., Grebel, E. K., Allison, R. J., et al. 2013, *The Astrophysical Journal*, 764, 73
- Riedel, A. R., Alam, M. K., Rice, E. L., Cruz, K. L., & Henry, T. J. 2017, *The Astrophysical Journal*, 840, 87
- Strassmeier, K. G., Fekel, F. C., Bopp, B. W., Dempsey, R. C., & Henry, G. W. 1990
- Sung, H. & Bessell, M. S. 2004, *The Astronomical Journal*, 127, 1014
- Venuti, L., Bouvier, J., Flaccomio, E., et al. 2014, *Astronomy & Astrophysics*, 570, A82
- Young, A., Skumanich, A., Stauffer, J. R., Bopp, B. W., & Harlan, E. 1989, *Astrophysical Journal, Part 1 (ISSN 0004-637X)*, vol. 344, Sept. 1, 1989, p. 427-436., 344, 427

Appendix A: Emission line profiles

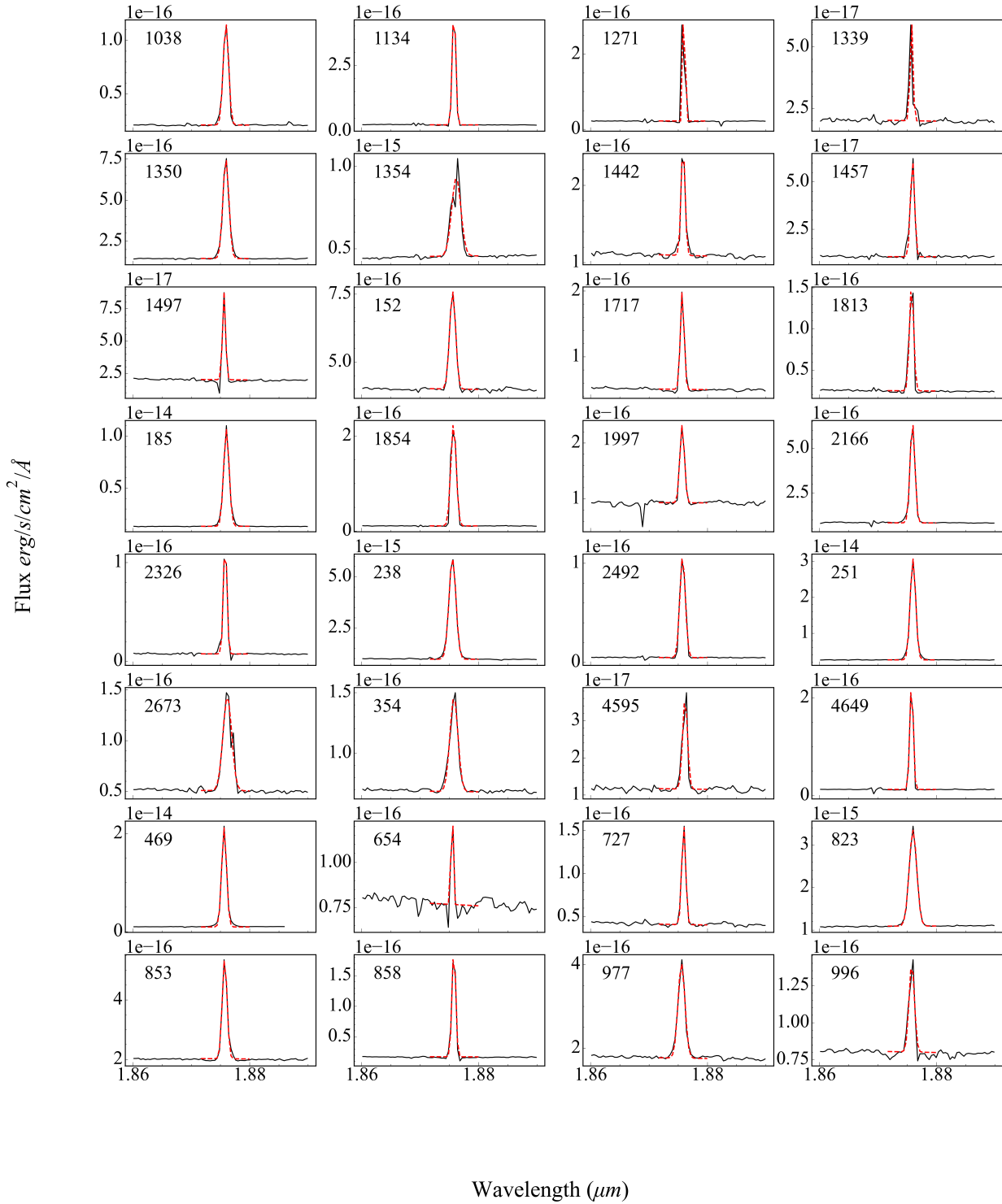


Fig. A.1: Pa_α emission line profile for each source. The best fitting Gaussian profile is shown as a red dashed line.

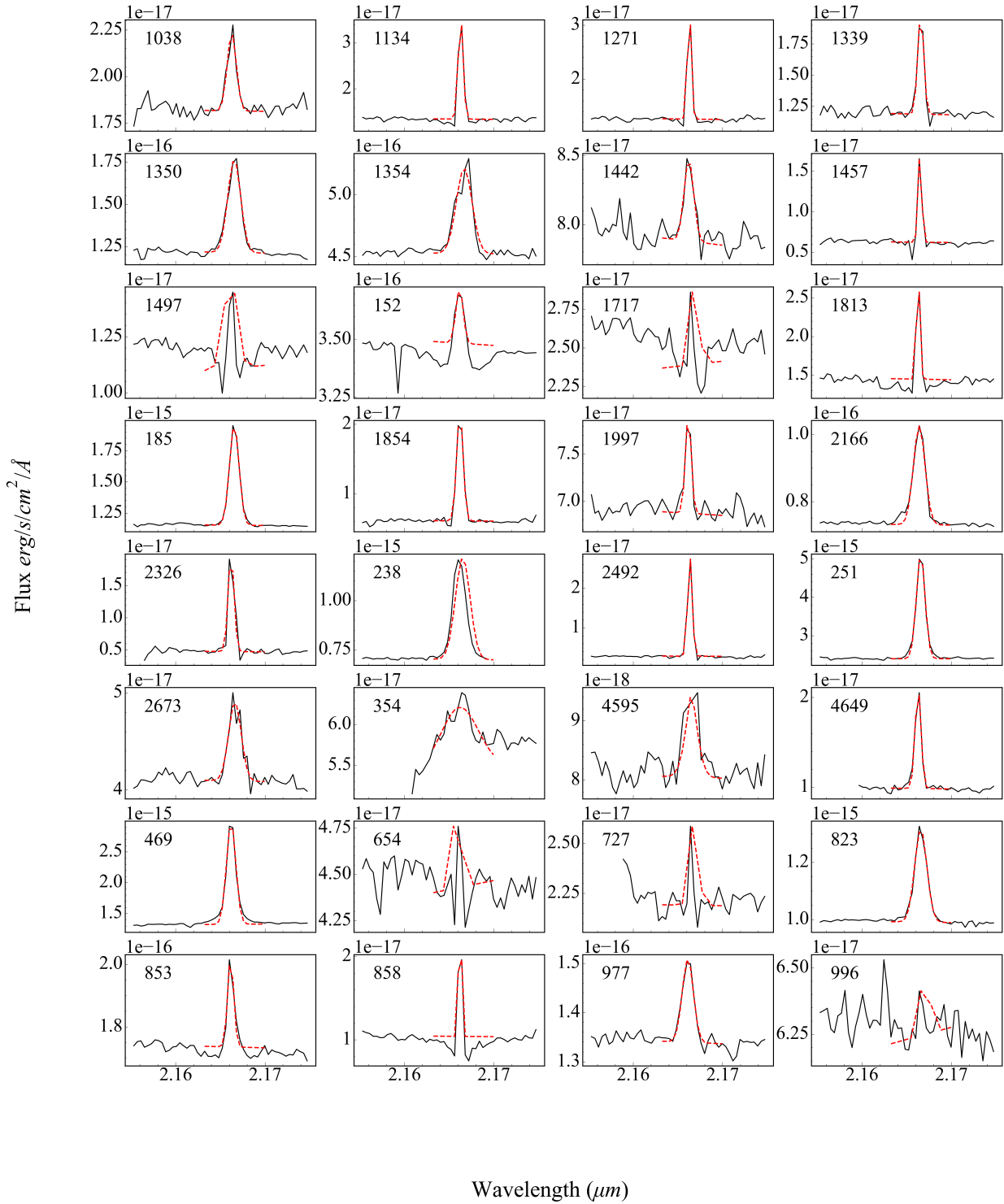


Fig. A.2: Br_γ emission line profile for each source. The best fitting Gaussian profile is shown as a red dashed line.

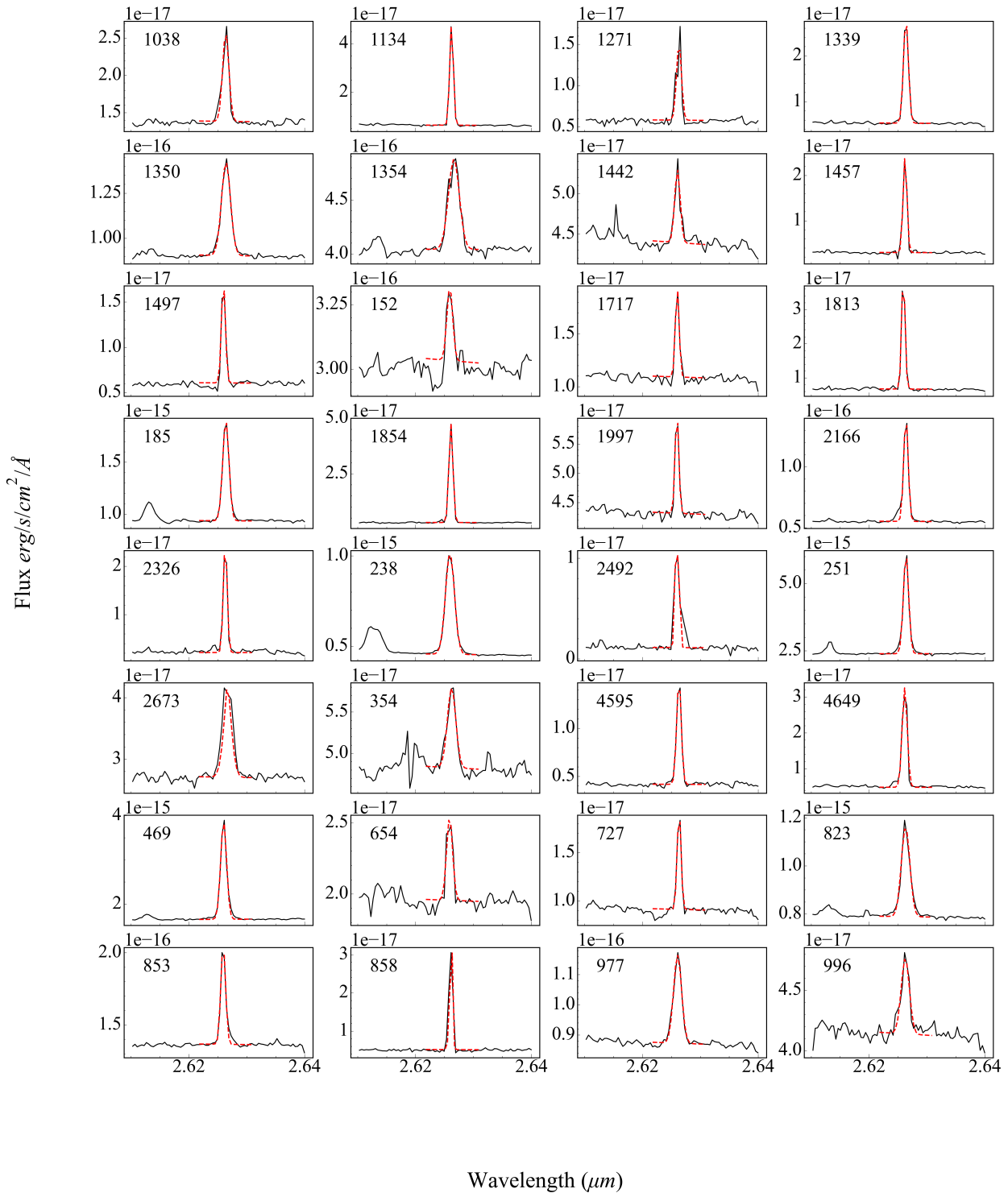


Fig. A.3: Br_{β} emission line profile for each source. The best fitting Gaussian profile is shown as a red dashed line.